AGU PUBLICATIONS

Geophysical Research Letters

RESEARCH LETTER
10.1002/2016GL071197

Key Points:
- We characterize Martian north polar strata with a new topographic metric more efficient at detecting periodicities than previous metrics
- We observe a ratio of stratigraphic periodicities consistent with nonlinear time-depth relationships controlled by astronomical forcing
- Coupling our observations with a published ice accumulation model supports evidence that the top 1 km of the NPLD was deposited over ~2 Myr

Supporting Information:
- Supporting Information S1
- Table S1

Correspondence to:
P. Becerra,
becerra@lpl.arizona.edu

Citation:
Becerra, P., M. M. Sori, and S. Byrne (2017), Signals of astronomical climate forcing in the exposure topography of the North Polar Layered Deposits of Mars, *Geophys. Res. Lett.*, *43*, doi:10.1002/2016GL071197.

Received 13 SEP 2016
Accepted 20 NOV 2016
Accepted article online 24 NOV 2016

Signals of astronomical climate forcing in the exposure topography of the North Polar Layered Deposits of Mars

Patricio Becerra[1], Michael M. Sori[1], and Shane Byrne[1]

[1]Lunar and Planetary Laboratory, University of Arizona, Tucson, Arizona, USA

Abstract Using high-resolution topography, we link the stratigraphy of layered ice deposits at the north pole of Mars to astronomically driven climate variability. Observations of trough exposures within these deposits are used to construct virtual ice cores at 16 sites, to which we apply wavelet analysis to identify periodicities in layer properties. To confidently relate these periodicities to climatic forcing, we identify overlapping dominant stratigraphic wavelengths and compare their ratios to that of the two dominant modes of insolation variability. The average ratio of stratigraphic wavelengths in the profiles is 1.9 ± 0.1, lower than the ratio of 2.3 between dominant insolation periodicities. A similar analysis of synthetic stratigraphic profiles created with a climate-driven model of ice and dust accumulation shows that this lower stratigraphic ratio is a natural consequence of time-variable ice accumulation rates.

1. Introduction and Background

The polar layered deposits (PLD) of Mars are kilometers thick stratified sequences of ice and dust that represent a geologically recent climate record of the planet. Models show that the northern deposits (NPLD, Figure 1a) likely accumulated during the last ~4–5 Myr [*Levrard et al.*, 2007; *Putzig et al.*, 2009; *Hvidberg et al.*, 2012], although some uncertainty remains. The PLD are dissected by a series of spiraling troughs that allow a view of their internal structure, first observed by the Mariner and Viking orbiters [*Murray et al.*, 1972; *Cutts*, 1973; *Cutts et al.*, 1976]. This layered structure (Figures 1b and 1c) is believed to be the result of variability in the accumulation of ice and/or dust, which has long been hypothesized to be controlled by shifts in insolation due to changes in Mars' orbital parameters (in particular changes in its argument of perihelion and obliquity, with periods ~51 kyr and ~120 kyr, respectively [*Murray et al.*, 1973; *Toon et al.*, 1980; *Cutts and Lewis*, 1982; *Howard et al.*, 1982; *Thomas et al.*, 1992; *Laskar et al.*, 2002; *Milkovich and Head*, 2005; *Hvidberg et al.*, 2012]). Despite the long-hypothesized link between orbital cycles and PLD accumulation, this connection remains unproven through direct observations and is one of the most important issues in Mars polar science today [*Clifford et al.*, 2013].

Terrestrial paleoclimate records have similarly been connected to changes in Earth's orbit, but the extent to which these changes control glacial variability is an open problem [*Hays et al.*, 1976; *Raymo and Huybers*, 2008; *Perron and Huybers*, 2009]. The current Martian climate system is much simpler than Earth's because of its thinner atmosphere and lack of oceans and biological activity. Additionally, any orbitally driven climate signal should be stronger on Mars because its obliquity and eccentricity oscillations have larger amplitudes [*Laskar et al.*, 2004]. Thus, although events like dust storms complicate the relationship between climate and stratigraphy [*Pollack*, 1979; *Toon et al.*, 1980; *Haberle*, 1986; *Zurek and Martin*, 1993], a correlation should be possible if enough time is recorded in the stratigraphy and is not removed by ablation [*Sori et al.*, 2014].

To test this correlation, an accurate description of the stratigraphic record and a detailed analysis of its periodicities are required. Due to their younger age and simpler stratigraphy compared to their southern counterpart, the NPLD have been the focus of the majority of research to date. Past studies have relied on the observed brightness of exposed layers to construct depth-varying stratigraphic signals and analyze their periodicities [*Laskar et al.*, 2002; *Milkovich and Head*, 2005; *Perron and Huybers*, 2009; *Fishbaugh et al.*, 2010a, 2010b; *Limaye et al.*, 2012]. Most authors agree that there is a dominant stratigraphic wavelength of 25–30 m in the upper 300–500 m of the NPLD [*Laskar et al.*, 2002; *Milkovich and Head*, 2005], although wavelet analysis [*Perron and Huybers*, 2009] showed little evidence for any periodicity in that wavelength range and instead discovered a periodic wavelength of ~1.6 m. The relationship between the brightness of exposed layers and their

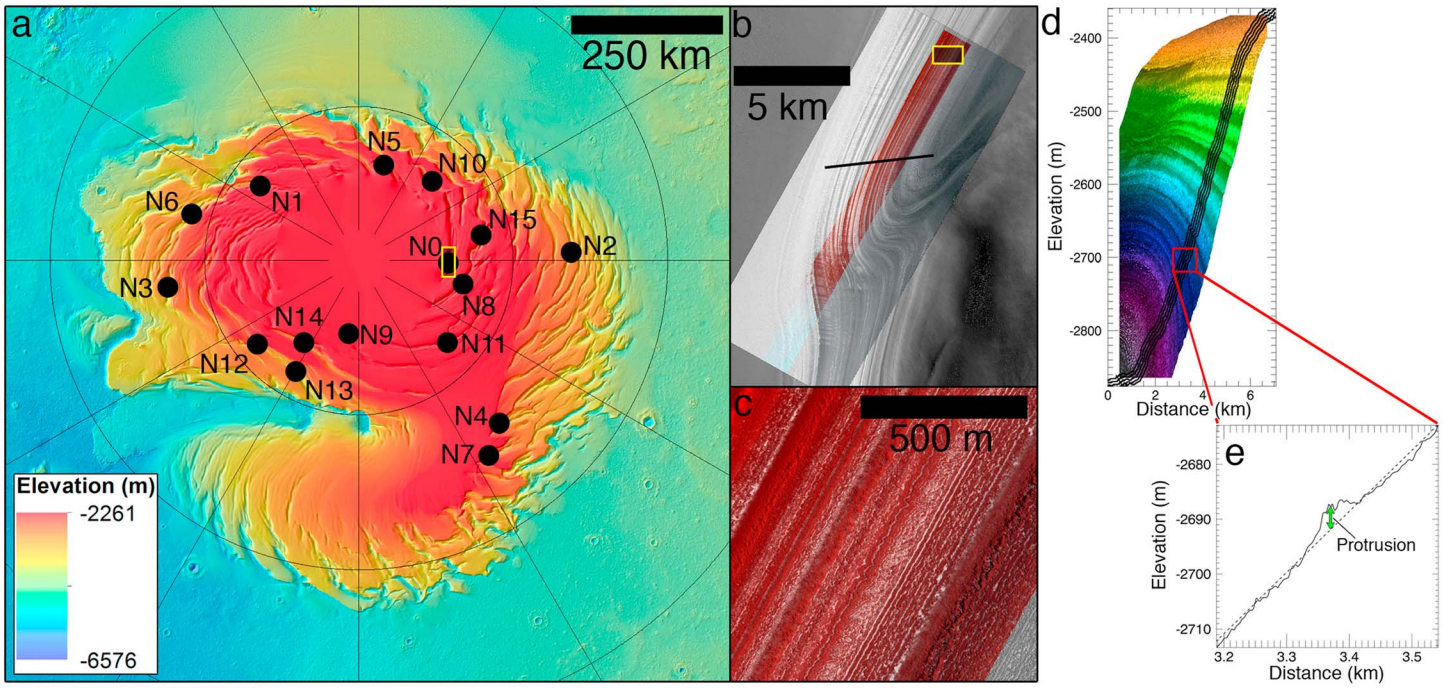

Figure 1. (a) Topographic map (Mars Orbiter Laser Altimeter) of Mars' NPLD. The black dots indicate our study sites. (b) HiRISE merged color image of site N0 (yellow box in Figure 1a) over a Context Camera (CTX) image. The black line represents the track of the profiles we extracted. (c) Zoomed-in view of yellow box in Figure 1b. (d) Perspective view of HiRISE DTM with 1-D topographic profiles drawn (black line in Figure 1b), which we used to extract protrusion and slope from the DTM and brightness from the orthoimages. (e) Schematic of the protrusion calculation.

underlying physical properties is complex and is influenced by factors that may not be directly related to layer composition, such as sublimation lags that cover the exposures [*Herkenhoff et al.*, 2007; *Becerra et al.*, 2016]. Therefore, an orbital signal may be too difficult to extract from brightness-based stratigraphy, even if present.

Using digital terrain models (DTMs) made from High-Resolution Imaging Science Experiment (HiRISE) [*McEwen et al.*, 2007] stereo imagery, *Fishbaugh et al.* [2010a] mapped the stratigraphy at one location on the NPLD. They argued that a morphologic/topographic description of the layers may be more appropriate than one based solely on layer brightness. Using HiRISE DTMs, *Becerra et al.* [2016] extracted 16 stratigraphic profiles based on the protrusion of exposed layers from the average slope of a trough wall and correlated 6 profiles throughout a large region of the NPLD. They suggest that layer protrusion is a proxy for layers' resistance to erosion and may have a simpler relationship to intrinsic layer properties than does brightness. Their results indicate that the combination of topography with brightness makes layer sequences easier to correlate, thereby improving the description of the exposed stratigraphic record.

Here we use wavelet analysis to study topography- and brightness-based stratigraphic profiles of layer exposures from across the NPLD and compare periodicities in the stratigraphy to those found in the insolation history. We interpret the relationship between these two by performing the same analysis on synthetic stratigraphies from models of NPLD accumulation [*Hvidberg et al.*, 2012] to test whether these models accurately predict the spectral properties of the NPLD.

2. Methods

2.1. Stratigraphic Profiles

At each of the 16 study sites shown in Figure 1, we analyzed three types of stratigraphic profiles: layer protrusion, local slope, and layer brightness versus depth. We extracted protrusion and slope from HiRISE DTMs [*Kirk et al.*, 2008; *Sutton et al.*, 2015]. The horizontal postspacing within these DTMs is 1 m, so that coupled with a typical scarp slope of ~10°, the typical vertical resolution is ~18 cm. To extract brightness, we use orthorectified HiRISE images, which represent "map view" renditions of the terrain, i.e. have all topographic and camera distortions removed, and match the DTMs pixel for pixel.

The protrusion profiles are the same as in *Becerra et al*. [2016]. Layer protrusion is the difference between a 1-D topographic profile (Figure 1d) of a trough wall taken from the DTM and a linear fit to that profile within a local window 350 m in length (Figure 1e). Although window size affects the absolute value of protrusion, its relative shape (i.e., the locations of peaks in the profile and their relative amplitudes) is unaffected. See *Becerra et al*. [2016] for details on the calculation of protrusion and caveats of its use as a stratigraphic property.

We measured local slope as the first derivative of the 1-D topographic profiles. Figures 2a and 2c show the protrusion and slope profiles for site N0. Protrusion and slope differ: protrusion is evaluated within a local window of a certain size, suppressing wavelengths larger than the window size and effectively acting as a high-pass filter of the topography; slope is differentiated topography over the smallest possible baseline (1 m pixel size) and thus contains shorter wavelengths but more noise. Although the same high-resistance beds can be identified in both protrusion and slope profiles, sequences that repeat with wavelengths of tens of meters are more easily detected in protrusion profiles. The brightness profiles are profiles of I/F (measured intensity (I) divided by solar irradiance when incidence angle is zero (F), such that $I/F = 1$ for a normally illuminated, perfectly diffuse reflector) extracted from the orthorectified images at the same locations as the topographic profiles (Figure 2e). To reduce noise caused by roughness along strike in all three data sets, we made representative profiles for each site by averaging five profiles separated from each other by 10 m along strike (Figure 1d) [*Becerra et al*., 2016].

The climate signal to which we compared the stratigraphic profiles is the noontime insolation during summer solstice at 85°N, calculated from the orbital solutions of *Laskar et al*. [2004] (provided every kyr for the past 20 Myr). For comparison with our stratigraphic profiles, we use the portion of the solution from 0 to 2 Ma (Figure 3a). *Levrard et al*. [2007] showed that it is unlikely the NPLD could have existed during the period of high obliquity before 5 Ma. Given that the NPLD troughs we study here only expose the uppermost 10–20% of the stratigraphic record, comparing our profiles with the 2 Ma insolation is reasonable.

2.2. Wavelet Analysis

We searched for periodicities in the stratigraphic signal by using wavelet transforms that decompose time-dependent series into their components in time-frequency space, determining not only the dominant modes of time variability but also how these vary in time [*Torrence and Compo*, 1998]. In the case of NPLD profiles, depth-varying profiles are transformed into depth-wavelength space, and the results are shown as 2-D images of spectral power, which we use to identify periodic layering in the stratigraphy and how it varies with depth. The wavelet transform is calculated through the convolution of the profile with a wavelet function. The wavelet power spectrum (WPS) is the square of the real portion of the transform and is plotted in the 2-D images of Figures 2b, 2d, 2f, 2h, 2j, and 2l (see supporting information for further details [*Torrence and Compo*, 1998; *Farge*, 1992]).

In order to be confident that peaks in the WPS represent real periodicities, we needed to assess the probability that a profile with similar periodicities could be produced at random, as high spectral power does not necessarily imply high statistical significance [*Torrence and Compo*, 1998; *Perron and Huybers*, 2009]. To estimate this probability, a random background noise signal is assumed to modulate the real profile. Paleoclimate records tend to follow a red noise background [*Mann and Lees*, 1996] (i.e., one in which spectral power density is proportional to wavelength squared). *Perron and Huybers* [2009] showed this to be true in NPLD brightness profiles, and we found that FFT power increases with wavelength and levels off at the longest wavelengths for brightness, protrusion, and slope (Figure S1). This is consistent with the simplest red noise distribution, an autoregressive process of order 1 (AR(1)), so such a distribution could be assumed to modulate the data.

We therefore tested the null hypothesis that the profiles have a mean power spectrum given by that of an AR(1) process [*Gillman et al*., 1963]. If a peak in the WPS is significantly above this background spectrum, we identified it as a true feature with a certain confidence level. We tested for such significance using a Monte Carlo procedure in which we construct 10,000 AR(1) series that are statistically similar to the data and calculate their WPS, allowing us to draw contours of confidence on the WPS of the data. As in previous studies [*Perron and Huybers*, 2009], we assumed significance where the real WPS has higher power than 95% of the simulated AR(1) profiles. The black curves overplotted on the WPS of Figure 2 show depth-wavelength

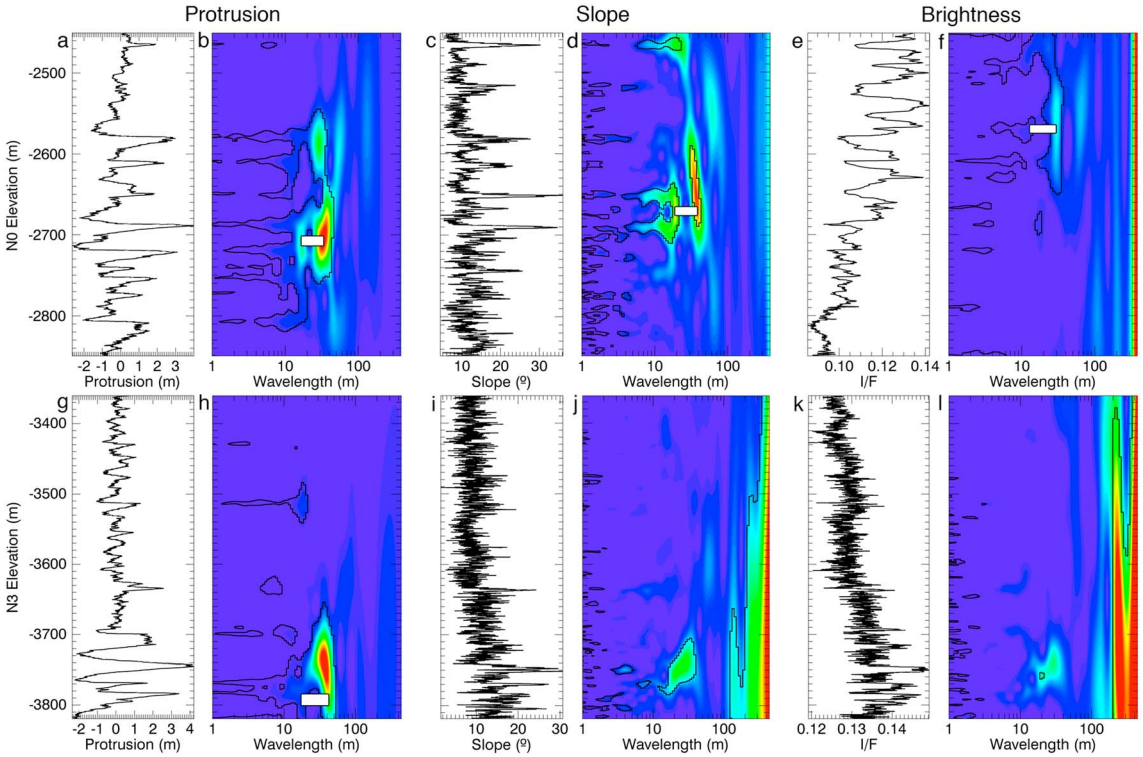

Figure 2. Stratigraphic profiles (line plots) and WPS (colored images) of sites N0 and N3. Warmer colors signify higher power. The black curves delineate the 95% confidence contours for red noise plotted over the WPS. Wavelength-depth regions within these contours are considered to have statistically significant spectral power. (a) Protrusion profile of site N0. (b) WPS of Figure 2a. The width of the white bar represents a ratio between dominant wavelengths of 1.94. (c) Local slope profile of site N0. (d) WPS of Figure 2c. White bar = ratio of 2. (e) I/F profile of site N0. (f) WPS of Figure 2e. White bar = ratio of 2.4. (g–l) Same as Figures 2a–2f but for site N3. White bar in 2 h = ratio of 2.33.

regions where spectral power is significant at the 95% confidence level (Figure S2 shows curves of 90 to 99% confidence for the N0 protrusion profile).

Sharp isolated peaks in the stratigraphic profiles produce significant power at only that depth at all wavelengths (e.g., see the peak at ~−2690 m in Figures 2a and 2b). We tested sinusoid signals with similar peaks artificially added and also found significant power at all wavelengths at the locations of such peaks (Figure S3). These sharp peaks do not appear in the random signals, so the data always appear to have significant power at these locations. Consequently, we do not interpret bands where significant power occurs at all wavelengths to represent real periodicities.

3. Results

Average NPLD accumulation rates can be estimated by comparing the ratio of two dominant bedding wavelengths to two orbital periodicities. For example, the ~5:1 ratio of the precession to eccentricity cycles of Earth has been observed in the rock record [*House*, 1995; *Schwarzacher*, 2000]. On Mars, *Lewis et al*. [2008] used this approach to relate a 10:1 ratio of stratigraphic wavelengths in outcrops at Becquerel crater to the ratio of the ~120 kyr obliquity period to its modulation timescale of ~1.2 Myr. In the case of the NPLD, inferred accumulation rates can be converted into an absolute age of the observed stratigraphy if one assumes that the deposits continue to accumulate today (i.e., fixing zero depth at zero age), for which there is evidence from crater size-frequency analysis [*Landis et al*., 2016]. However, absolute dating of long stratigraphic sequences may be complicated by unconformities in the record [*Smith et al*., 2016].

In each profile's WPS, we found the two most dominant wavelengths at the same elevation that have power that exceeds 95% confidence (i.e., within the black contours in Figure 2). As a measure of the uncertainty in the identification of these wavelengths, we calculated the half width at half maximum of these peaks. We restricted measurements to peaks in the WPS that extend over depth intervals that include at least two full

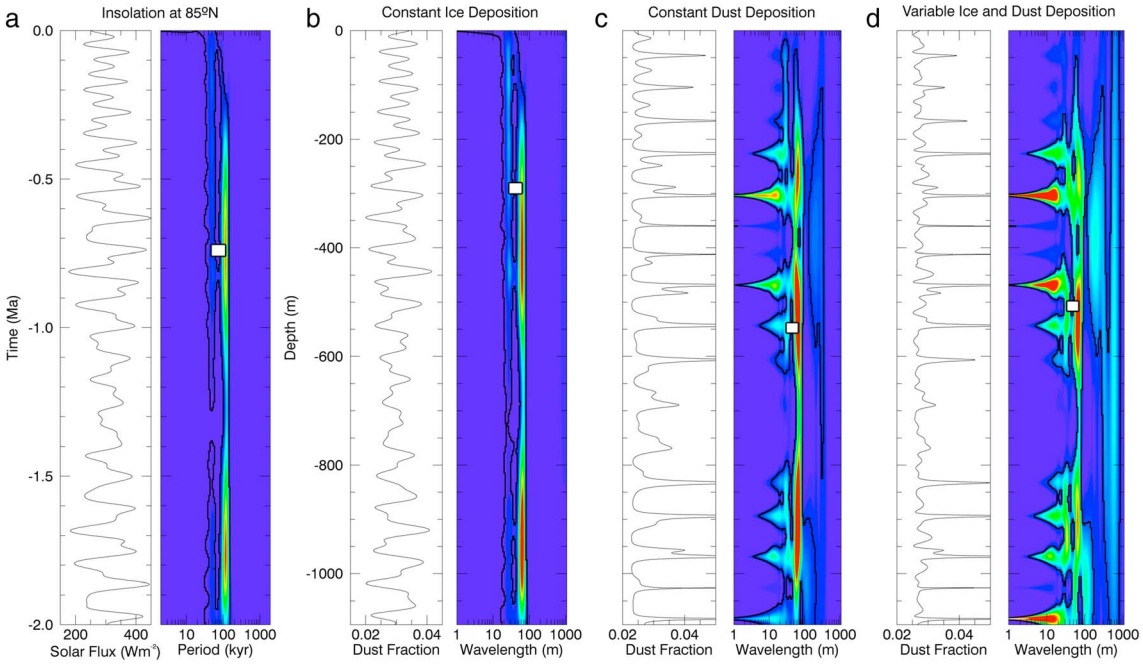

Figure 3. (a) Variation of the peak solar flux on Mars at 85°N over the last 5 Myr (left) and its WPS (right). The width of the white bar on the WPS image represents a ratio of ~2.3 between the ~51 kyr precession cycle of the argument of perihelion and the ~120 kyr obliquity oscillation. (b–d) Synthetic stratigraphic profiles of dust to ice ratio created with the model of *Hvidberg et al.* [2012] and their WPS. Figure 3b shows constant ice deposition rate but time-varying dust deposition rate. White bar = ratio of 2.19. Figure 3c shows constant dust deposition rate but time-varying ice deposition rate. White bar = ratio of 1.91. Figure 3d shows that both rates vary with time. White bar = ratio of 1.97.

wavelengths, and consider a strong detection when a peak extends over three wavelengths; i.e., a 30 m signal must have significant power over a depth range of at least 60 m to be considered for further analysis and over 90 m to be considered a strong detection of periodicity (we henceforth refer to these as the 2λ and 3λ criteria). For example, at site N0 (Figure 2b) the dominant wavelengths are 33 ± 7.29 m and 17 ± 2.35 m over depth ranges from -2630 m to -2750 m (~4 wavelengths) and from -2670 m to -2810 m (~8 wavelengths), respectively. The ratio of the long to short dominant wavelengths at this site is 1.94 ± 0.51 and is represented in Figure 2b by the width of the white horizontal bar. To ensure that our method is not susceptible to detecting significant power from spectral leakage, we calculated the WPS and 95% confidence contour of a signal constructed by adding red noise to a sinusoid of similar length to the data and discontinuous at the ends and found leakage to be negligible (see supporting information [*Torrence and Compo*, 1998; *Arrillaga and Watson*, 2003]).

The results for all significant wavelengths throughout all sites are summarized in Table 1. Thirteen of the 16 protrusion profiles have two overlapping significant wavelengths detected that meet the 2λ criterion and 8 that meet 3λ. The slope data set has four sites above 2λ and just one above 3λ, and there are only two brightness profiles that meet either criterion. As shown in Figures 2a–2f and explained above, site N0 has overlapping significant periodicities in all three data sets. While this makes it a useful site for explaining the results of our analysis, it does not represent a typical case within our sample of 16 sites. Figures 2g–2l show the analysis of all three properties for site N3, which is a more typical case than N0. At N3, the pair of wavelengths identified in the slope profile do not meet the 2λ criterion, and there are no dominant wavelengths in the brightness profile that exceed 95% confidence for any meaningful depth range. Results analogous to Figure 2 for all other sites are in Figure S5.

The eight protrusion profiles with pairs of dominant wavelengths that meet 3λ have a mean ratio of 1.87 ± 0.17. In the slope data set, the only strong detection has a ratio of 1.89 ± 1.17 between wavelengths, and the mean ratio of the two sites with significant brightness periodicities is 2.21 ± 0.64. When including all profiles of any type, the mean ratio between dominant periodicities that meet 3λ is 1.93 ± 0.20 and the median is 1.89 ± 0.11.

In addition to the dominant wavelengths reported in Table 1, a number of short wavelengths (1–5 m) exceed the 95% confidence level in the slope and brightness profiles (Figures 2d, 2f, 2j, and 2l). However, these peaks

Table 1. Dominant Periodicities and Ratios of Stratigraphic Profiles of the NPLD, of the Insolation Signal, and of the Three Model Scenarios[a]

	Long-Wavelength Signal			Short-Wavelength Signal			Ratio of Dominant Wavelengths	
Profile Location/Model Scenario	λ (m)	Error	Number of λ's in Depth Range	λ (m)	Error	Number of λ's in Depth Range	Ratio	Propagated Error
Protrusion								
N0	**33**	**7.29**	**3.64**	**17**	**2.35**	**8.24**	**1.94**	**0.51**
N1	**48**	**7.91**	**3.33**	**27**	**2.93**	**3.70**	**1.78**	**0.35**
N2	**42**	**6.58**	**3.45**	**23**	**3.05**	**6.09**	**1.83**	**0.37**
N3	**42**	**7.34**	**4.05**	**18**	**2.86**	**4.44**	**2.33**	**0.55**
N4	**51**	**5.53**	**4.90**	**29**	**5.98**	**7.59**	**1.76**	**0.41**
N5	**59**	**12.20**	**3.22**	**31**	**9.40**	**3.55**	**1.90**	**0.70**
N6	68	10.78	2.50	27	6.70	7.41	2.52	0.74
N7	48	12.59	2.08	19	4.94	10.53	2.53	0.93
N8	54	9.07	2.96	27	5.63	7.78	2.00	0.54
N9	**17**	**3.84**	**4.12**	**9**	**1.23**	**5.00**	**1.89**	**0.50**
N12	71	10.91	2.11	41	5.79	10.00	1.73	0.36
N14	70	14.70	3.00	40	7.84	2.75	1.75	0.50
N15	**30**	**3.35**	**7.67**	**20**	**3.65**	**10.00**	**1.50**	**0.32**
2λ mean	48.69	2.56		25.23	1.47		1.96	0.15
3λ mean	**40.25**	**2.56**		**21.75**	**1.63**		**1.87**	**0.17**
Slope								
N0	38	6.37	2.63	19	2.91	4.47	2.00	0.45
N1	27	4.31	2.41	14	2.22	2.14	1.93	0.43
N2	23	9.08	2.17	8	1.42	3.53	2.71	1.16
N6	**17**	**10.03**	**3.53**	**9**	**1.70**	**3.33**	**1.89**	**1.17**
2λ mean	26.25	3.89		12.50	1.07		2.13	0.44
3λ mean	**17**	**10.03**		**9**	**1.70**		**1.89**	**1.17**
Brightness								
N0	**29**	**4.09**	**6.90**	**12**	**5.72**	**5.83**	**2.42**	**1.20**
N2	**20**	**3.28**	**3.50**	**10**	**1.63**	**3.50**	**2.00**	**0.46**
2λ, 3λ mean	**24.50**	**2.62**		**11.00**	**2.97**		**2.21**	**0.64**
			Average ratios of all three data sets			2λ mean	2.02	0.14
						2λ median	1.93	0.15
						3λ mean	**1.93**	**0.20**
						3λ median	**1.89**	**0.11**
Insolation	Period (kyr)	Error		Period (kyr)	Error			
85°N	115.00	16.40		50.00	6.50		2.30	0.44
Stratigraphic Model								
Constant ice	59.00	11.30	16.95	27.00	4.05	37.04	2.19	0.53
Constant dust	63.00	9.05	15.87	33.00	4.74	24.24	1.91	0.39
Variable ice and dust	67.00	10.40	8.96	34.00	5.71	5.88	1.97	0.45

[a]In the list of stratigraphic profiles, values in bold correspond to periodicities that exceed the 3λ criterion, and all periodicities listed exceed at least the 2λ criterion. See text for explanation of detection criteria and uncertainty calculations. See supporting information for a detailed spreadsheet indicating the specific depth ranges of dominant wavelengths in each profile to compare with each WPS.

do not meet even the 2λ criterion; i.e., the power at these wavelengths exceeds the 95% contour only in small pockets of depth comparable in size to the wavelengths themselves. This result is consistent with previous brightness-based [*Perron and Huybers*, 2009] and topography-based [*Limaye et al.*, 2012] studies. The former found a significant signal centered on a wavelength of ~1.6 m, also in small pockets of depth within the profile (see their Figure 4), while the latter found several sets of fine beds 1–2 m in thickness. Comparing the number of significant signals we found using protrusion to those we found using slope or brightness shows that the protrusion data set allows for the detection of dominant wavelengths not readily apparent in the data sets that these prior studies used.

The two dominant modes of oscillation of the insolation signal, corresponding to the obliquity (~120 kyr) and precession of the argument of perihelion (~51 kyr) are clearly visible in the WPS of those data (Figure 3a). To compare equivalent quantities, we measured the peak periodicities and their uncertainties using the same

methods applied to the stratigraphic wavelengths (Table 1). The ratio between the measured dominant periods is 2.3 ± 0.44.

At this point we can summarize four important results. First, the protrusion profiles reveal periodicities not apparent in brightness profiles and at more than one wavelength. Second, although both long and short dominant wavelengths have a significant spread, their ratio is similar over many locations on the NPLD (Table 1). Third, this ratio of dominant periodicities in the stratigraphy is systematically lower than that in the insolation record. Finally, discontinuous sequences with periodicities at wavelengths of 1–5 m may also exist, as previously shown by *Perron and Huybers* [2009].

4. Discussion and Conclusions

A lower periodicity ratio in the stratigraphy than in the insolation implies either that NPLD formation is not primarily driven by orbital control (although no other periodicities are apparent in Figure 3a) or that a nonlinear relationship between insolation (time) and accumulation (depth) in the NPLD leads to a lower ratio in the stratigraphy. In order to interpret our results and test whether the latter is plausible, we applied wavelet analysis to synthetic stratigraphic profiles created with an insolation-forced model of NPLD formation developed by *Hvidberg et al*. [2012]. In this model, the annual net deposition rate of ice is controlled by the north polar surface temperature, and the annual net deposition rate of dust depends on the temperature difference between the north pole and the equator. Surface temperatures are calculated by a local energy balance using the insolation solution of *Laskar et al*. [2004]. Using the best fit model parameters found by *Hvidberg et al*. [2012], we evaluate three accumulation scenarios that result in three different stratigraphic profiles: one in which the ice deposition rate is constant but the dust deposition rate varies with time, one in which the reverse is true, and one in which both dust and ice deposition rates vary with time. See the supporting information for details on our application of this model and *Hvidberg et al*. [2012] for the algorithm.

The dominant wavelengths of the synthetic stratigraphies are shown in the last three rows of Table 1 and in Figures 3b–3d. The WPS of the stratigraphy formed by a constant ice deposition rate differs very little from that of the insolation, displaying a ratio of 2.19 ± 0.53 (Figure 3b). However, scenarios with a varying ice deposition rate have spectral signatures that are similar to that observed in the stratigraphic data, with ratios of 1.91 ± 0.39 (constant dust deposition rate, Figure 3c) and 1.97 ± 0.45 (variable dust deposition rate, Figure 3d). The comparison of model results to the observed wavelength ratios therefore implies that a variation of ice deposition rate is necessary to match the spectral properties of the observed stratigraphy, while changes in the deposition of dust appear to have only a minor effect.

From our analysis it is clear that different scenarios of accumulation forced by the same periodic climate signal can result in spectrally distinct stratigraphies. The history of accumulation that the model of *Hvidberg et al*. [2012] suggests (with dust and ice varying with time) correctly predicts the periodic characteristics we measured within NPLD stratigraphy. Here we use this model to show that the observed difference between the periodicity ratios of the insolation and the stratigraphy can be reconciled by this nonlinear time-depth relationship. However, future research is needed to know if other historical solutions would also correctly predict the same spectral characteristics.

The two model scenarios that are spectrally similar to the data have net annual deposition rates that vary between -0.35 mm/yr and 0.72 mm/yr (negative ice deposition rates result in removal of previously deposited ice layers and formation of a dust lag). The mean net deposition rate for the 2 Myr time period is 0.54 mm/yr. The top of the N0 column (Figures 2a–2f) is ~130 m below the surface of the NPLD [*Hvidberg et al*., 2012]. Assuming that the surface represents present day, with the deposition rate function of the third scenario (variable rates with the best fit parameters of *Hvidberg et al*. [2012]) the N0 profiles can be dated to extend from ~960 kyr to ~215 kyr, consistent with the range quoted by *Hvidberg et al*. [2012] for a slightly longer column at the same location. *Becerra et al*. [2016] correlated the stratigraphic sequence of N0 to five sites (N1, N6, N10, N8, and N15; Figure 1), so these age estimates are probably reasonable for those locations as well. According to this model, ~1.1 km of material has been deposited over the last 2 Myr. Nevertheless, it is likely that there is an unconformity above the section that we mapped at N0, corresponding to the hiatus between the ABb_3 and ABb_1 units [*Tanaka et al*., 2008; 2012; *Smith et al*., 2016], which the model of *Hvidberg et al*. [2012] does not reproduce. Therefore, this age is a lower limit, and the real age requires the addition of the unknown duration represented by such an unconformity.

The characteristic ratio between stratigraphic wavelengths that we have observed can be used to test the results of future modeling efforts, as any climate-driven model of NPLD formation must reproduce dominant wavelengths in the stratigraphy that have similar ratios to those that we have observed. If the NPLDs are formed primarily as a result of orbital forcing, then our results show that the relationship between time and depth must be nonlinear. In addition, the geographic variation in stratigraphic wavelengths indicates that deposition rates can be spatially variable while still being driven by the same climatic forcing. Our results show that while a link between climate and stratigraphy requires a variable ice deposition rate, observations are consistent with either a constant or variable dust deposition rate.

Acknowledgments

The authors thank the HiRISE team for acquiring and processing the data used in our study. These data are available in the NASA Planetary Data System (pds.nasa.gov). We especially thank Sarah Sutton, Michael Berube, Nicholas Shea, and Aaron Kilgallon for their efforts in producing the DTMs used in this study. We also thank Isaac Smith and an anonymous reviewer for their helpful comments that improved this manuscript. Support for this work came from grant NNX13AO55H of the NASA Earth and Space Science Fellowship (Becerra) and NASA's Mars Reconnaissance Orbiter project (HiRISE).

References

Arrillaga, J., and N. R. Watson (2003), *Power System Harmonics*, John Wiley, Ltd. Chichester, U. K.

Becerra, P., S. Byrne, M. M. Sori, S. Sutton, and K. E. Herkenhoff (2016), Stratigraphy of the north polar layered deposits of Mars from high-resolution topography, *J. Geophys. Res. Planets*, *121*, 1445–1471, doi:10.1002/2015JE004992.

Clifford, S. M., et al. (2013), Introduction to the fifth Mars Polar Science special issue: Key questions, needed observations, and recommended investigations, *Icarus*, *225*(2), 864–868, doi:10.1016/j.icarus.2013.04.005.

Cutts, J. A. (1973), Nature and origin of layered deposits of the Martian polar region, *J. Geophys. Res.*, *78*, 4231–4249, doi:10.1029/JB078i020p04231.

Cutts, J. A., and B. H. Lewis (1982), Models of climate cycles recorded in Martian polar layered deposits, *Icarus*, *50*, 216–244.

Cutts, J. A., K. R. Blasius, G. A. Briggs, M. H. Carr, R. Greeley, and H. Masursky (1976), North polar region of Mars: Imaging results from Viking 2, *Science*, *194*(4271), 1329–1337, doi:10.1126/science.194.4271.1329.

Farge, M. (1992), Wavelet transforms and their applications to turbulence, *Annu. Rev. Fluid Mech.*, *24*, 395–457.

Fishbaugh, K. E., C. S. Hvidberg, S. Byrne, P. S. Russell, K. E. Herkenhoff, M. Winstrup, and R. Kirk (2010a), First high-resolution stratigraphic column of the Martian north polar layered deposits, *Geophys. Res. Lett.*, *37*, L07201, doi:10.1029/2009GL041642.

Fishbaugh, K. E., S. Byrne, K. E. Herkenhoff, R. L. Kirk, C. Fortezzo, P. S. Russell, and A. Mcewen (2010b), Evaluating the meaning of "layer" in the Martian north polar layered deposits and the impact on the climate connection, *Icarus*, *205*(1), 269–282, doi:10.1016/j.icarus.2009.04.011.

Gillman, D. L., F. J. Fuglister, and J. M. Mitchell (1963), On the power spectrum of "red noise", *J. Atmos. Sci.*, *20*, 182–184.

Haberle, R. M. (1986), Interannual variability of global dust storms on Mars, *Science*, *234*, 459–461, doi:10.1126/science.234.4775.459.

Hays, J. D., J. Imbrie, and N. J. Shackleton (1976), Variations in the Earth's orbit: Pacemaker of the ice ages, *Science*, *194*(4), 1121–1132, doi:10.1126/science.194.4270.1121.

Herkenhoff, K. E., S. Byrne, P. S. Russell, K. E. Fishbaugh, and A. S. McEwen (2007), Meter-scale morphology of the north polar region of Mars, *Science*, *317*(5845), 1711–1715, doi:10.1126/science.1143544.

House, M. R. (1995), Orbital forcing timescales: An introduction, *Geol. Soc. Lond. Spec. Publ.*, *85*(1), 1–18, doi:10.1144/GSL.SP.1995.085.01.01.

Howard, A. D., J. A. Cutts, and K. R. Blasius (1982), Stratigraphic relationships within Martian polar cap deposits, *Icarus*, *50*, 161–215.

Hvidberg, C. S., K. E. Fishbaugh, M. Winstrup, A. Svensson, S. Byrne, and K. E. Herkenhoff (2012), Reading the climate record of the Martian polar layered deposits, *Icarus*, *221*(1), 405–419, doi:10.1016/j.icarus.2012.08.009.

Kirk, R. L., et al. (2008), Ultrahigh resolution topographic mapping of Mars with MRO HiRISE stereo images: Meter-scale slopes of candidate Phoenix landing sites, *J. Geophys. Res.*, *113*, E00A24, doi:10.1029/2007JE003000.

Landis, M. E., S. Byrne, I. J. Daubar, K. E. Herkenhoff, and C. M. Dundas (2016), A revised surface age for the North Polar Layered Deposits of Mars, *Geophys. Res. Lett.*, *43*, 3060–3068, doi:10.1002/2016GL068434.

Laskar, J., B. Levrard, and J. F. Mustard (2002), Orbital forcing of the Martian polar layered deposits, *Nature*, *419*, 375.

Laskar, J., A. C. M. Correia, M. Gastineau, F. Joutel, B. Levrard, and P. Robutel (2004), Long term evolution and chaotic diffusion of the insolation quantities of Mars, *Icarus*, *170*, 343–364, doi:10.1016/j.icarus.2004.04.005.

Levrard, B., F. Forget, F. Montmessin, and J. Laskar (2007), Recent formation and evolution of northern Martian polar layered deposits as inferred from a Global Climate Model, *J. Geophys. Res.*, *112*, E06012, doi:10.1029/2006JE002772.

Lewis, K. W., O. Aharonson, J. P. Grotzinger, R. L. Kirk, A. S. McEwen, and T.-A. Suer (2008), Quasi-periodic bedding in the sedimentary rock record of Mars, *Science*, *322*(5), 1532–1536, doi:10.1126/science.1161870.

Limaye, A. B. S., O. Aharonson, and J. T. Perron (2012), Detailed stratigraphy and bed thickness of the Mars north and south polar layered deposits, *J. Geophys. Res.*, *117*, E06009, doi:10.1029/2011JE003961.

Mann, M. E., and J. M. Lees (1996), Robust estimation of background noise and signal detection in climatic time series—Springer, *Clim. Change*, *33*(3), 409–445.

McEwen, A. S., et al. (2007), Mars Reconnaissance Orbiter's High Resolution Imaging Science Experiment (HiRISE), *J. Geophys. Res.*, *112*, E05S02, doi:10.1029/2005JE002605.

Milkovich, S. M., and J. W. Head (2005), North polar cap of Mars: Polar layered deposit characterization and identification of a fundamental climate signal, *J. Geophys. Res.*, *110*, E01005, doi:10.1029/2004JE002349.

Murray, B. C., L. A. Soderblom, J. A. Cutts, and R. P. Sharp (1972), Geological framework of the south polar region of Mars, *Icarus*, *17*, 328–345.

Murray, B. C., W. R. Ward, and S. C. Yeung (1973), Periodic insolation variations on Mars, *Science*, *180*(4086), 638–640, doi:10.1126/science.180.4086.638.

Perron, J. T., and P. Huybers (2009), Is there an orbital signal in the polar layered deposits on Mars? *Geology*, *37*(2), 155–158, doi:10.1130/G25143A.1.

Pollack, J. B. (1979), Climatic change on the terrestrial planets, *Icarus*, *37*(3), 479–553.

Putzig, N. E., R. J. Phillips, B. A. Campbell, J. W. Holt, J. J. Plaut, L. M. Carter, A. F. Egan, F. Bernardini, A. Safaeinili, and R. Seu (2009), Subsurface structure of Planum Boreum from Mars Reconnaissance Orbiter Shallow Radar soundings, *Icarus*, *204*(2), 443–457.

Raymo, M. E., and P. L. Huybers (2008), Unlocking the mysteries of ice ages, *Nature*, *451*, 284–85, doi:10.1038/nature06589.

Schwarzacher, W. (2000), Repetitions and cycles in stratigraphy, *Earth Sci. Rev.*, *50*, 51–75.

Smith, I., N. E. Putzig, J. W. Holt, and R. J. Phillips (2016), An ice age recorded in the polar deposits of Mars, *Science*, *352*, 1075–78.

Sori, M. M., J. T. Perron, P. Huybers, and O. Aharonson (2014), A procedure for testing the significance of orbital tuning of the Martian polar layered deposits, *Icarus*, *235*(C), 136–146, doi:10.1016/j.icarus.2014.03.009.

Sutton, S., M. Chojnacki, A. Kilgallon, and H. R. I. S. E. Team (2015), Precision and accuracy of simultaneously collected HiRISE digital terrain models, *Lunar Planet. Sci. Conf.*, *46*, 3010.

Tanaka, K. L., J. A. P. Rodriguez, J. A. Skinner, M. C. Bourke, C. M. Fortezzo, K. E. Herkenhoff, E. J. Kolb, and C. H. Okubo (2008), North polar region of Mars: Advances in stratigraphy, structure, and erosional modification, *Icarus*, *196*, 318, doi:10.1016/j.icarus.2008.01.021.

Tanaka, K. L., and C. M. Fortezzo (2012), Geologic Map of the North Polar Region of Mars, U.S. Geological Survey Scientific Investigations Map 3177, scale 1:2,000,000.

Thomas, P., S. Squyres, K. Herkenhoff, A. Howard, and B. Murray (1992), Polar deposits of Mars, in *Mars*, pp. 767–795, Univ. Ariz. Press, Tucson, Ariz.

Toon, O. B., J. B. Pollack, W. Ward, J. A. Burns, and K. Bilski (1980), The astronomical theory of climatic change on Mars, *Icarus*, *44*(3), 552–607.

Torrence, C., and G. P. Compo (1998), A practical guide to wavelet analysis, *Bull. Am. Meteorol. Soc.*, *79*(1), 61.

Zurek, R. W., and L. J. Martin (1993), Interannual variability of planet-encircling dust storms on Mars, *J. Geophys. Res.*, *98*, 3247–3259, doi:10.1029/92JE02936.